Masotti, R., Maguire, P. K. H., Mechie, J. (1996): On the upper mantle beneath the Kenya Rift. - Geophysical Journal International, 126, 2, pp. 579—592.

DOI: http://doi.org/10.1111/j.1365-246X.1996.tb05311.x

Geophys. J. Int. (1996) **126**, 579–592

On the upper mantle beneath the Kenya Rift

R. Masotti,[1,*] P. K. H. Maguire[1,†] and J. Mechie[2,†]

[1]*Department of Geology, University of Leicester, University Road, Leicester* LE1 7RH, *UK*
[2]*Geophysikalisches Institut, Universität Karlsruhe, Hertzstrasse* 16, 76187, *Karlsruhe, Germany*

Accepted 1996 April 4. Received 1996 April 1; in original form 1995 March 9

SUMMARY

During the Kenya Rift International Seismic Project (KRISP 90) a 450 km long E–W seismic-refraction/wide-angle-reflection profile involving the deployment of 250 instruments was shot across the Kenya Rift. A reflected phase recorded between distances of 260 and 350 km from a 1000 kg shot at the western end of the line in Lake Victoria has been interpreted as originating from about 60 km beneath the western margin of the rift.

Detailed processing of this phase has resulted in defining its polarity in relation to the first-arrival diving wave at the same range. Extensive kinematic and dynamic modelling shows there is a high-velocity zone at depths below 60 km under the western flank of the rift. We cannot exclude the presence of a layered alternating high–low-velocity structure as found in the upper mantle beneath the northern part of the N–S seismic profile along the rift axis.

Constraints from xenolith studies indicate that anisotropy may explain the high velocity found beneath the reflecting horizon (≥ 8.40 km s^{-1}). Petrological modelling shows that if the anisotropy is due to the preferred orientation of olivine crystals, then either a transverse isotropic structure, in which the '*a*' and '*c*' axes are randomly orientated in the horizontal plane, or an orthorhombic structure, in which the fast '*a*' axis is orientated along the direction of the E–W seismic line, is possible. The reflection could also be caused by a pre-rift structure associated with the Proterozoic collisional orogen involving the Mozambique Orogenic Belt and the Archaean Nyanza Craton, whose contact is subparallel to and lies about 70 km to the west of the Tertiary rift. The evidence presented here delimits the lateral extent of the upper-mantle region of anomalously low-velocity material that is confined to below the surface expression of the rift itself at depths below 60 km.

Key words: Kenya Rift, seismic modelling, upper mantle.

1 INTRODUCTION

One of the objectives of KRISP 90 was to detail the upper-mantle structure beneath the Kenya Rift Valley, where the rifting process is still active (Fig. 1).

It is generally accepted that rifting episodes are associated with magmatic activity whose origin resides in the lithospheric upper mantle or in the asthenosphere. Previous geophysical studies in Kenya have demonstrated large gravity and heat-flow anomalies, indicating the presence of anomalous mantle material or partial melt beneath the rift axis. A structural high has been modelled in the upper mantle, with the Moho rising from 38 km underneath the rift flanks to 30 km beneath the rift axis along the cross-rift line (Fig. 1) (Maguire *et al.* 1994). A close relationship has been suggested between asthenospheric upwelling and penetrative magmatism as driving forces for lithospheric rifting (Bhattacharji & Koide 1987).

This paper describes and interprets a phase 'd_1', reflected from a discontinuity below the Moho recorded during KRISP 90 on the cross-rift line (Fig. 1) on the section from the Lake Victoria shot point (VIC) at the western end of the profile; the section from which d_1 returns is indicated in Fig. 1. Similar phases have also been detected on the KRISP 90 east-flank line (Prodehl *et al.* 1994) and the KRISP 90 axial line, where two phases reflected from depths of respectively, 40–45 km and 60–65 km, within the uppermost mantle have been identified (Keller *et al.* 1994). Discontinuities within the upper mantle in rift zones have also been identified elsewhere, for example in the Afar depression and the Red Sea (Mooney

* Now at: Bullard Laboratories, Cambridge University, UK.
† Now at: GeoForschungsZentrum Potsdam, Germany.

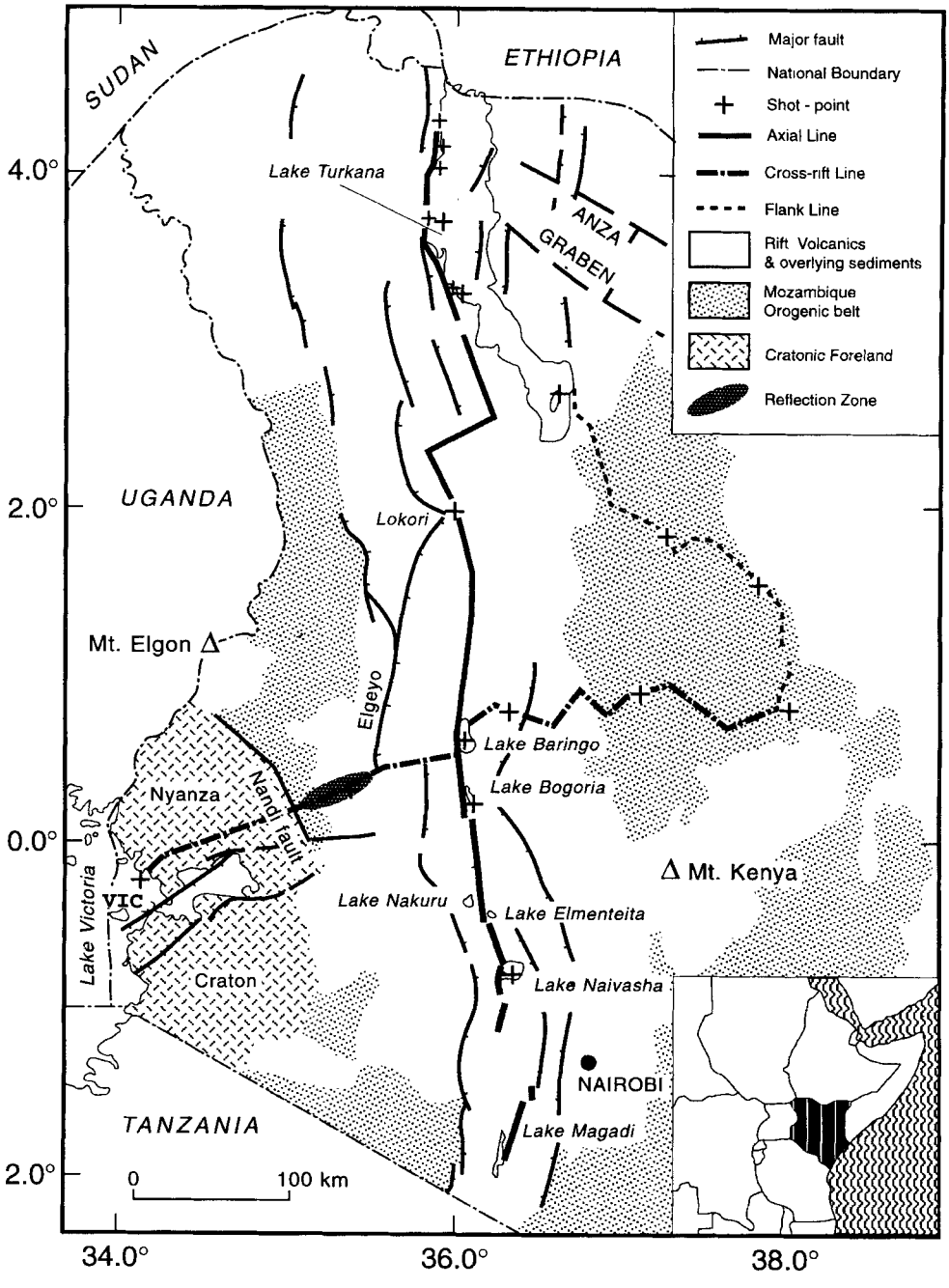

Figure 1. Location map of KRISP 90 explosion seismic profiles. The reflection zone indicates the section from which the d_1 discussed in the text returns.

et al. 1985; Prodehl 1985; Mechie, Prodehl & Koptschalitsch 1986; Makris & Ginzburg 1987).

The d_1 phase has been the subject of further processing and analysis to define its polarity, in order to determine whether a low-velocity zone (LVZ) exists in the upper mantle beneath the reflector. Studies of lithospheric structure elsewhere (Hirn *et al.* 1971; Kind 1974; Cassell & Fuchs 1979; Burmakov *et al.* 1987; Ansorge, Blundell & Mueller 1992) have revealed thin layers of both high and low velocity, explained via changes in either composition (Blundell 1992) or physical state (Fuchs 1983; Mechie, Fuchs & Altherr 1994). The interpretation of the KRISP 90 axial line has revealed a low-velocity layer between two high-velocity layers at a depth of between 50 and 65 km beneath the northern-central part of the profile (Keller *et al.* 1994), and for this reason it was important to study the polarity of phase d_1.

If we recognize that this phase has the same polarity as the first '*d*' arrival, *d* being the diving wave beneath the Moho, we can interpret such polarity as resulting from an increase in velocity across the reflector. The results may be compared with those from a number of long profiles within rifts that have provided information from reflectors below the Moho (Keller *et al.* 1994).

The seismic velocities derived from the present analysis have been compared with values determined from petrological modelling. The elastic properties of individual minerals can be used

to define the seismic velocities at a certain pressure and temperature for a given assemblage of these minerals. Mineralogical compositions are derived from xenolith studies (Henjes-Kunst & Altherr 1992), and a possible geotherm for the continental crust is based on a conductive model after Pollack & Chapman (1977).

2 THE SEISMIC DATA

The data studied have been recorded along the cross-rift line (Fig. 1), a 450 km profile between the equator and 1 °N, from the 1000 kg underwater Lake Victoria (VIC) shot at the western end of the line.

A detailed description of the interpretation of the cross-rift line can be found in Maguire *et al.* (1994), which contains a complete record section for the shot point VIC and from which the present crustal model is obtained.

The upper-mantle reflection d_1 is shown in two 'windows' extracted from the VIC record section, the seismograms being normalized and band-pass filtered (1–20 Hz) (Figs 2 and 3). For the following reasons we believe that this d_1 phase is an upper-mantle reflection and not a converted or scattered phase:

(1) if we omit the upper-mantle reflector in the model then we have no energy in the theoretical seismograms (see Section 5.2 below) where the phase d_1 should occur;

(2) although the d and d_1 phases are both observed in an area with complex crustal structure, both phases appear to be correlatable in a consistent and coherent fashion;

(3) along the rift axis itself and beneath the north-east flank of the rift, similar phases from uppermost-mantle reflectors have been recognized (Keller *et al.* 1994; Prodehl *et al.* 1994).

3 METHODS

The phase investigated is observed at a distance of 260–350 km from Lake Victoria. The quality of the data required detailed processing to be undertaken before enabling a comparison of the polarity of the reflection with the sub-Moho diving wave at the same offset. A decrease in velocity across the reflector would produce a reflection of opposite polarity to the first arrival. With a velocity increase, the polarity should be the same as that of the first arrival, as long as the reflection is still undercritical. Beyond the critical point the phase of the reflection starts to change, and eventually, at large distances, it will again have an opposite polarity to that of the first arrival. The distance over which the phase change occurs depends on the velocity contrast. For large velocity contrasts it changes over a fairly short range, whereas for mantle-reflected events involving small velocity contrasts it usually occurs over a large distance.

4 PROCEDURE

4.1 Processing

Band-pass frequency filtering improved the quality of the recorded seismograms. This was designed to enhance the crustal phases. The d_1 phase was first detected on these trace-

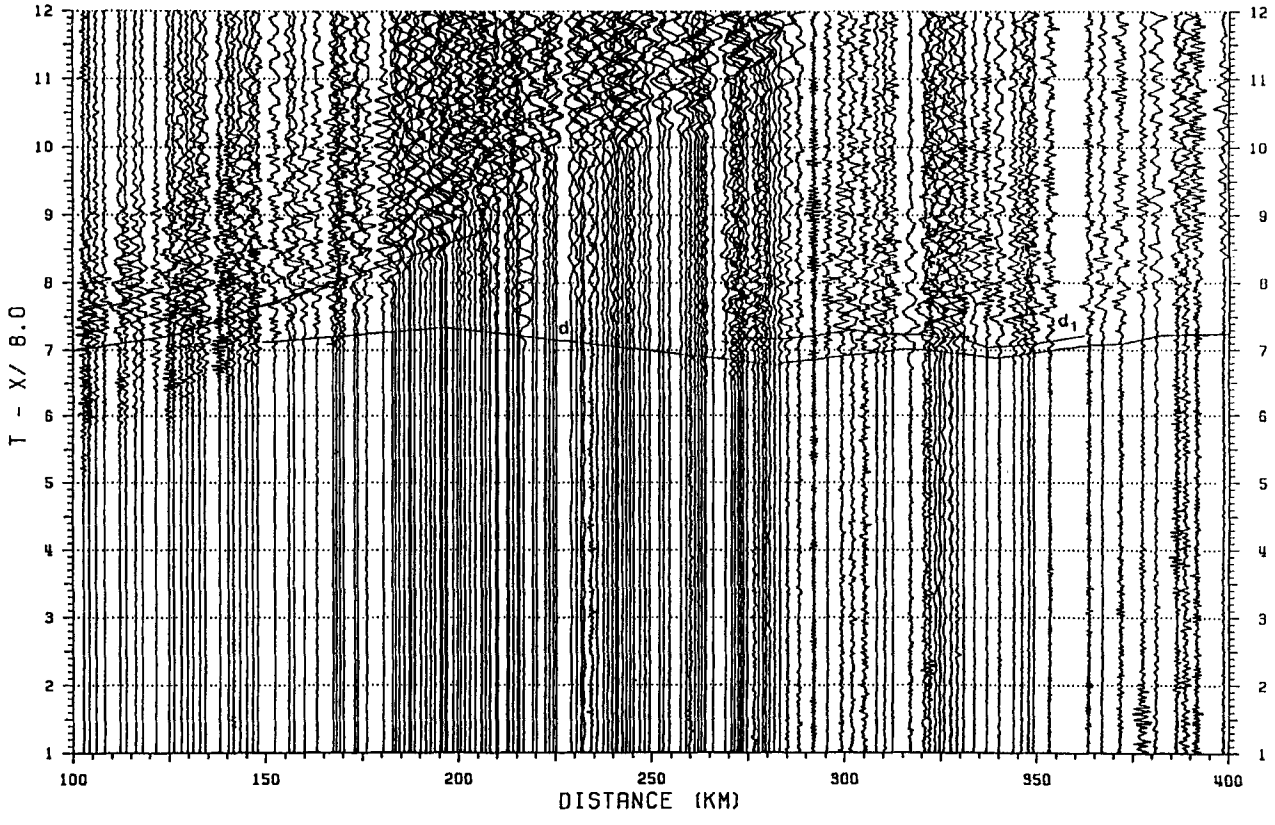

Figure 2. Record section for the Lake Victoria (VIC) shot point. Reducing velocity = 8.0 km s^{-1}. Band-pass filter 1–20 Hz. The modelled travel time picks for phases d and d_1, derived from the cross-rift line model of Maguire *et al.* (1994), are shown.

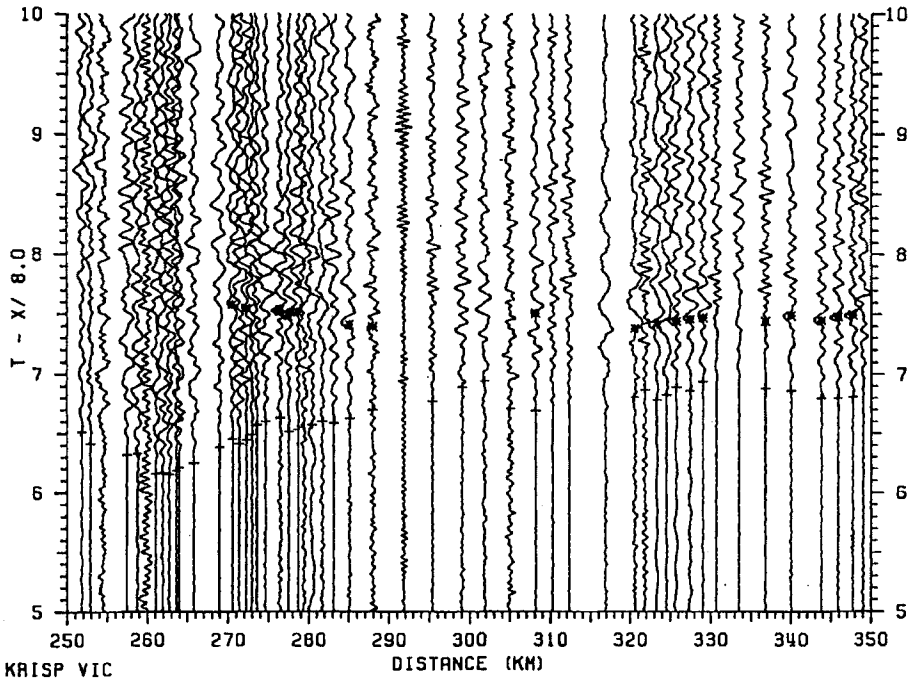

Figure 3. Record section for the Lake Victoria (VIC) shot point emphasizing phases d and d_1. Reducing velocity = 8.0 km s^{-1}. Band-pass filter 1–20 Hz. The observed travel time picks for phases d and d_1 are shown.

normalized band-pass filtered sections, and, together with the preceding first arrival, was extracted for further processing, in particular correlated adaptive noise cancellation (CANC) filtering (Hattingh 1988) and subsequent stacking.

4.2 CANC filtering

CANC was first developed as an extension of adaptive noise cancelling (Widrow & Hoff 1960; Widrow *et al.* 1975, 1976). CANC was initially designed to remove interference noise, random noise and linear or non-linear drift from a time-series using adaptive filters instead of fixed filters.

Fig. 4 (modified from Hattingh 1988) illustrates the CANC procedure. The primary input, D, contains the signal, S_0, and the noise, n_0. The reference input, X, contains the same signal plus a permitted delay and/or scale change, S_1, and noise, n_1, which is assumed to be uncorrelated with n_0. The reference input is adaptively filtered to produce the filter output, Y, which is a least-squares estimate of $D=S_0+n_0$. The filter output is subtracted from the primary input to give the system output or error, E. The error is then fed back into the adaptive filter and used to adjust the filter weights. Since n_0 is uncorrelated with the filter input $X=S_1+n_1$, the filter output is a least-squares estimate of the signal S (Kirk 1989).

The filter requires various input parameters, which are, following Hattingh (1988) and Kirk (1989), as follows.

L: the filter length. This should be set to twice the ratio of the signal-bandwidth-to-frequency resolution of the filter. Values from 25 to 38 samples were used following spectral analysis of the signal.

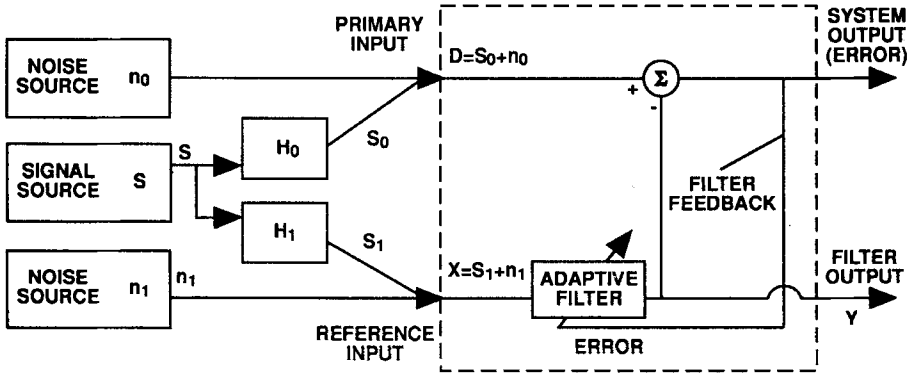

Figure 4. Correlated adaptive noise cancelling concept (CANC); modified from Hattingh (1988). H_0 and H_1 represent the introduction of allowable delays and/or scale factors.

μ: the convergence rate. Long filters with small convergence rates provide the greatest signal resolution. Values were set between 0.001 and 0.0001.

I: the number of iterations. The CPU time required increases with increasing I. Between 20 and 40 iterations were sufficient.

CANC filtering of wide-angle seismic data is ideal for enhancing separate signals from one shot point recorded at one recording site. In the present case, with signals recorded at a large distance from a single shot, we are assuming a correlation between the recorded phase at two adjacent recorders (spacing 0.3–3.8 km), but with uncorrelated noise. Noise spectra in the region, both from present and previous studies (Henry 1987) show that, in general, dominant noise frequencies (10–30 Hz) are higher than the signal frequency (0–10 Hz). Reasonable surface-noise velocities result in the dominant noise wavelength being significantly less than the station spacing.

CANC filtering can perform satisfactorily if there is a small phase shift between reference and input signal (Kirk 1989). As suggests by Kirk (1989) from synthetic data tests, the noisier signal should be on the primary input. Referring to Fig. 4 it can be seen that the reference input is adaptively filtered to become similar to the primary input. The system output power will be high if the noise power on the primary input signal is high.

Where possible, the signal closest to the shot was used as the reference signal. For very noisy signals, the reference and input signals were reversed to improve the output quality.

We analysed the d phase within a 1 s (200 sample) time-window starting at 6 s reduced time (for a reducing velocity of 8.0 km s^{-1}). The d_1 phase was analysed within a window of 2 s length.

The results are presented for selected traces for ranges between 260 and 350 km from the VIC shot point.

The derived cross-correlation function between the time windowed CANC-filtered traces provides an estimate of the time shift necessary to achieve the greatest similarity. The accepted time shift was always less than a wavelet cycle. Each CANC-filtered pair of traces has been cross-correlated with the input traces and only those with a cross-correlation >60 per cent were accepted.

Following CANC filtering and the subsequent time shifting, the best data sets were stacked. An example of the filtered and resultant stacked seismograms is shown in Fig. 5(a) for location numbers between 31 and 42 for phase d_1 and in Fig. 5(b) for the same location numbers for the d phase, between 320 and 344 km from VIC. The stacked seismogram for each group of traces is shown at the right-hand side of each figure.

For every location-number group the final output shows a d_1 phase with the same polarity as the first arrival d.

In order to quantify the similarity in each group between the d and the d_1 phases, cross-correlation has been carried out between d and d_1, as well as between d and an inverted d_1 phase for each group of location numbers. The result for traces in the critical range (between 312 and 345 km from VIC, using location numbers between 27 and 42 for d and between 27 and 45 for d_1) is shown in Fig. 6. A similar result is also determined for the group of traces in the undercritical range.

The measures of similarity suggest that the optimum result is achieved when cross-correlating the d phase with the d_1 phase, rather than the inverted d_1 phase, i.e. the polarity of the two phases may be taken to be the same, and the d_1 phase results from an increase in acoustic impedance in the uppermost mantle.

5 INTERPRETATION

5.1 Ray tracing

Prior to the polarity analysis, Maguire *et al.* (1994) modelled the reflector d_1 via ray tracing. They required a reflector at a depth of 55 km beneath the western margin of the rift (between about 140 and 160 km from VIC) to generate the high-amplitude phase d_1 immediately after phase d on the VIC record section. A reflector at a depth of about 50 km is also identified beneath the flank line to the north-east (Prodehl *et al.* 1994).

Maguire *et al.* (1994) arbitrarily suggested that the reflection resulted from a positive impedance contrast, consistent with the present flank-profile model. Beneath the axis of the rift the anomalously low-velocity material immediately beneath the Moho was modelled to a depth of at least 60 km. This is consistent with the axial-profile model, which identified a boundary with a small impedance contrast at this depth south of Lake Baringo (Keller *et al.* 1994). It is also consistent with the recent model derived from teleseismic data (Green *et al.* 1991). On further examination of the VIC data set it is just possible that the reflector identified beneath the flank of the rift continues beneath the rift itself. This reflector would be equivalent to the one modelled at about 60 km depth along the axial line (Keller *et al.* 1994).

The new evidence presented here increases confidence in the picking of both d and d_1. d_1 appears to occur at about 7.5 s reduced travel time ($V_R = 8.0$ km s^{-1}) between 280 and at least 350 km from VIC (Fig. 2b). The d_1 picks obtained in the present study are somewhat later than those obtained in Maguire *et al.* (1994), which has necessitated the d_1 reflector being placed at a greater depth.

The revised picked phases d and d_1 were again modelled using the MacRay package (Luetgert 1992), based on the ray-tracing algorithm of Červený, Molotkov & Pšenčík (1977). The velocity structure above 55 km depth has not been changed from the final model of Maguire *et al.* (1994). Perturbation of the models has shown that once the phase correlation has been fixed, resolution of the relevant velocity and depth to interface may be accepted as better than 1 per cent and 5 per cent, respectively.

Two different models are kinematically acceptable, one with and one without the presence of a LVZ (Figs 7a and b). In the former case the reflection arises from the base of the LVZ.

At about 350 km distance, the travel-time difference between the d and d_1 phases is about 0.5 s and the two phases have very similar apparent velocities. For this reason, and in order to move the theoretical critical point to around 280 km distance, a LVZ was introduced. In this case the observed travel times and amplitudes can be matched using a velocity of 8.4 km s^{-1} under the reflector, together with a 4 km thick LVZ between 55 and 59 km depth and an average velocity in the LVZ of 7.7 km s^{-1}. The velocity in the LVZ is taken from the axial line model.

However, the observed travel times and amplitudes can also be fitted within the error limits without the necessity of a LVZ. In this case a velocity of 8.65 km s^{-1} beneath the reflector,

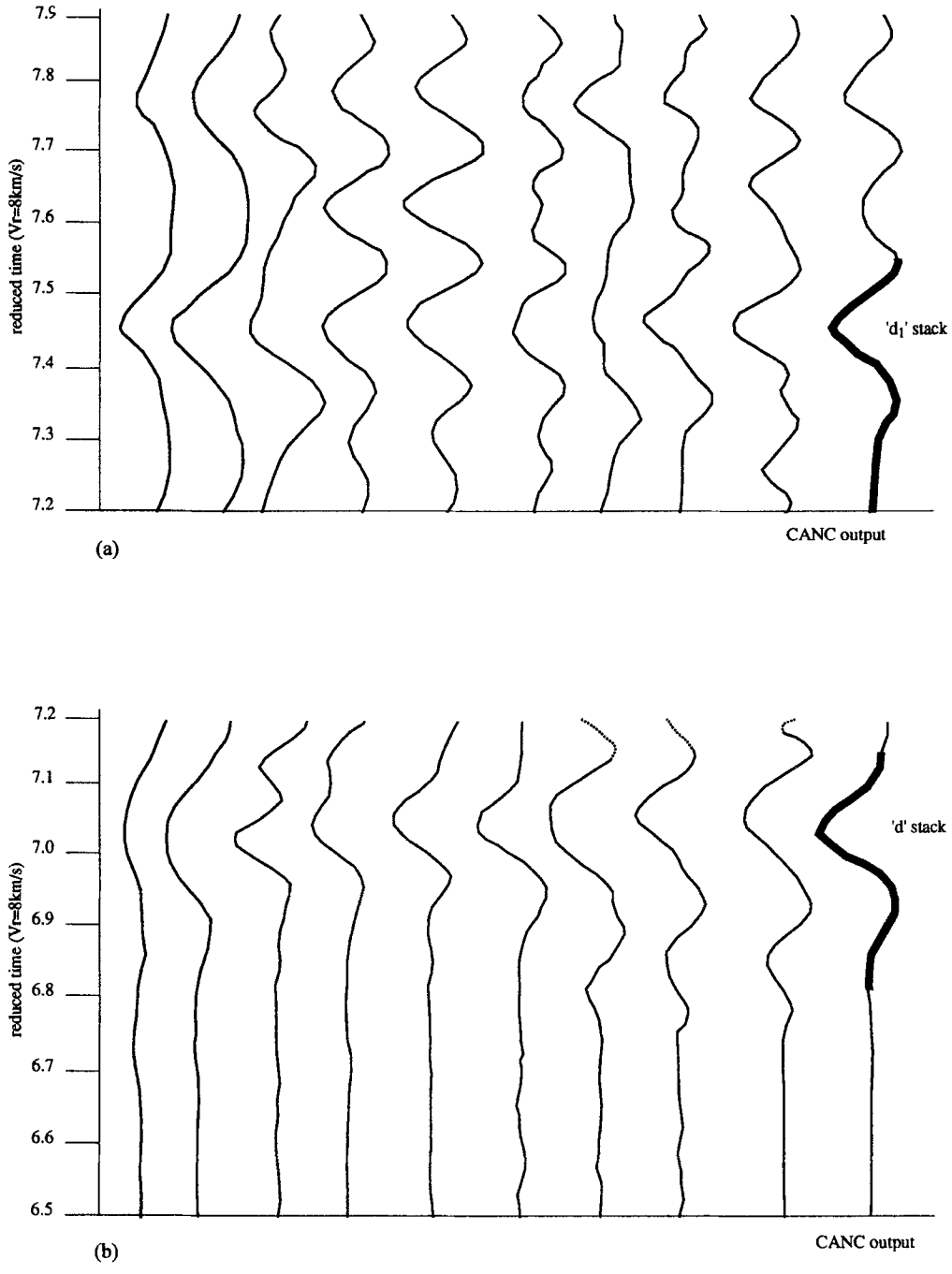

Figure 5. (a) CANC output seismograms for location numbers 31–42 and their stack for the d phase. Each trace shown is the CANC output from two adjacent seismograms, the display showing sequential CANC output traces. (b) CANC output seismograms for location numbers 31–42 and their stack for the d_1 phase. Each trace shown is the CANC output from two adjacent seismograms, the display showing sequential CANC output traces. It should be noted that the filter length may be different and in some cases the traces used are not the same for d and d_1.

which should now be at 63 km depth, is required. The resultant theoretical critical point is at 304 km distance from VIC. Correcting for the sphericity of the Earth (Mereu 1967), the velocity below the reflector decreases to 8.56 km s^{-1}.

Both models fit the travel times equally well. In both cases the ray coverage on the reflector is limited to the distance range 100–180 km from VIC, i.e. to the west of the surface expression of the rift. In the next section we will use the amplitude ratios between the d and d_1 phases to try to discriminate between the two models.

5.2 Synthetic seismogram modelling

We have computed synthetic seismograms for the two seismic models using two methods: the ray method (Červený *et al.* 1977) and finite-difference modelling (Kelly *et al.* 1976; Sandmeier 1990); only the latter is discussed here. The synthetic record sections in Fig. 8 were computed by a finite-difference technique for 2-D heterogeneous elastic media, which enables a complete description of the seismic wavefield. The phase in between d and d_1 in Fig. 8(a), arising from the top of the LVZ,

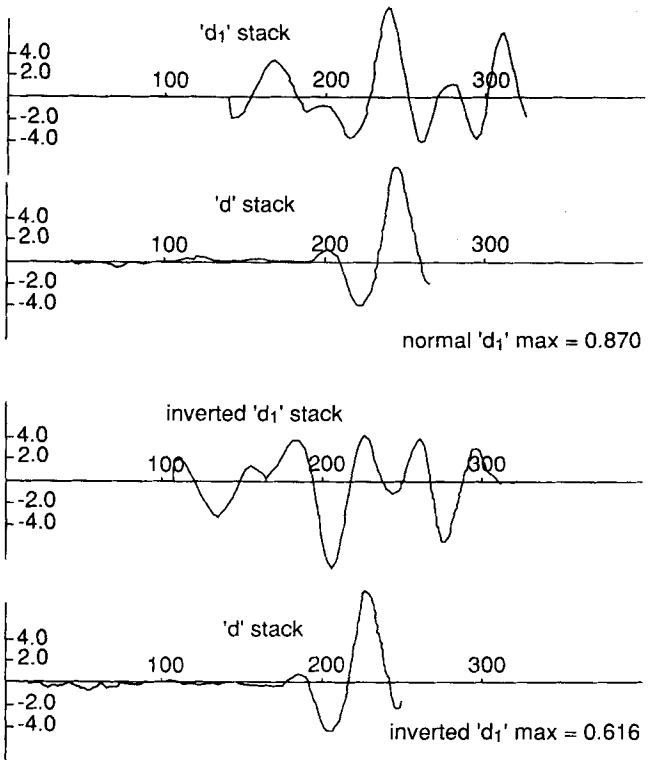

Figure 6. Example of CANC output stacked seismograms d cross-correlated with a time shifted d_1 (location number 27–42 for d and 27–45 for d_1). Top: d with a normal polarity d_1; bottom: d with an inverted polarity d_1.

would be strongly attenuated for a 2nd-order velocity change here.

Finite-difference synthetic-seismogram modelling enables a complete response of the model to the input source function. It can automatically account for the relative amplitudes of the various arrivals, and includes contributions from converted waves, Rayleigh waves, head waves and diffractions from fault zones. It is, of course, subject to limitations, e.g. model resolution and grid spacing. It can enable the matching of calculated to observed times in regions where 2-D kinematic ray tracing breaks down. According to Červený (1985), 'the ray method, of course, cannot compete in the accuracy of computations with the reflectivity method', and the finite-difference technique may be considered as a 2-D reflectivity method.

We digitized our ray-traced model with a grid spacing of 40 m for the calculations. The dominant frequency for which we calculated the seismograms was 4 Hz, according to the stability conditions of the finite-difference modelling (Kelly *et al.* 1976) and the analysis of the power spectra for the mantle phases. This analysis showed that relatively high frequencies (up to 10 Hz) are preserved beyond the anomalous upper mantle, which has no strong damping effect on the P waves.

5.3 Amplitude ratio versus offset calculation

The maximum and minimum values of the observed amplitudes were automatically measured for the chosen phase within a selected time window. Due to considerable scatter of the observed amplitude data, probably caused by varying site response at the recording stations, we preferred, instead of 'true' amplitudes, to use amplitude ratios of the two phases (d_1/d). Peak-to-peak amplitudes were also measured for the theoretical d and d_1 phases from both record sections (Fig. 8), and amplitude ratios of the two phases (d_1/d) were thus calculated for both the model with the LVZ (Fig. 8a) and the model without the LVZ (Fig. 8b).

A comparison of the amplitude ratios of the synthetic seismograms using the two velocity functions (with and without the LVZ) shows that the model with the LVZ produces amplitude ratios slightly higher than the observed ones, while the model without the LVZ produces values somewhat too low before 280 km distance (Fig. 9). The d and d_1 phases apparently merge beyond 330 km from VIC on the synthetic section.

It should be noted that these amplitude ratios have been derived using isotropic layered models. If, as is proposed below, the high-velocity layer at about 60 km depth is anisotropic, with preferred orientation of olivine crystals, then the amplitude ratios shown here may be up to 20 per cent in error in the undercritical range and up to 5 per cent in error in the overcritical range.

The two models thus fit the observed amplitude ratios with more or less equal quality (Fig. 9). Considering the difficulty in defining the exact position of the critical point for the d_1 phase, the calculated amplitude ratios lie within the scatter of the observed ratios. For the finite-difference model without the LVZ the critical point is at about 300 km from VIC; for that with the LVZ it is at about 280 km from VIC.

An eastward dip on the reflector of 5° would move the critical point by no more than 30 km, still achieving a satisfactory travel-time fit. It is apparent that a range of models between the two endmembers presented can be considered to fit the travel-time and amplitude data. Appropriate variations in the thickness of the LVZ, depth of the interfaces, and seismic velocities may achieve the desired fit.

Although it is therefore not possible to exclude the presence of a LVZ, the seismic modelling does constrain the velocity beneath the reflector at about 8.4 ± 0.1 km s^{-1} at a depth of 59.0 ± 2.0 km in the model with the LVZ, and at about 8.6 ± 0.1 km s^{-1} at a depth of 63.0 ± 2.0 km in the model without the LVZ.

As mentioned in Section 5.1, it is possible that there is a reflector across the rift, but the velocity underneath it along the axis (7.8–7.9 km s^{-1}) is less than the one we find. In either case the relatively high velocity underneath the flank of the rift adjacent to lower velocities underneath the rift axis must be explained. The possible presence of a LVZ must also be discussed.

5.4 Petrological modelling

A technique that allows the evaluation of the seismic velocity of a rock at a known pressure and temperature from estimated elastic properties of individual minerals is described in detail in Fuchs (1983) and Mechie *et al.* (1994). Knowing the mineral composition of a rock and *in situ* temperature and pressure, then P- and S-wave velocities can be calculated. We have applied this method to the modelling of the seismic velocity in the uppermost mantle beneath the western flank of the rift valley.

The temperature–depth values are estimated from Pollack & Chapman (1977) for a continental geotherm. Normal heat-

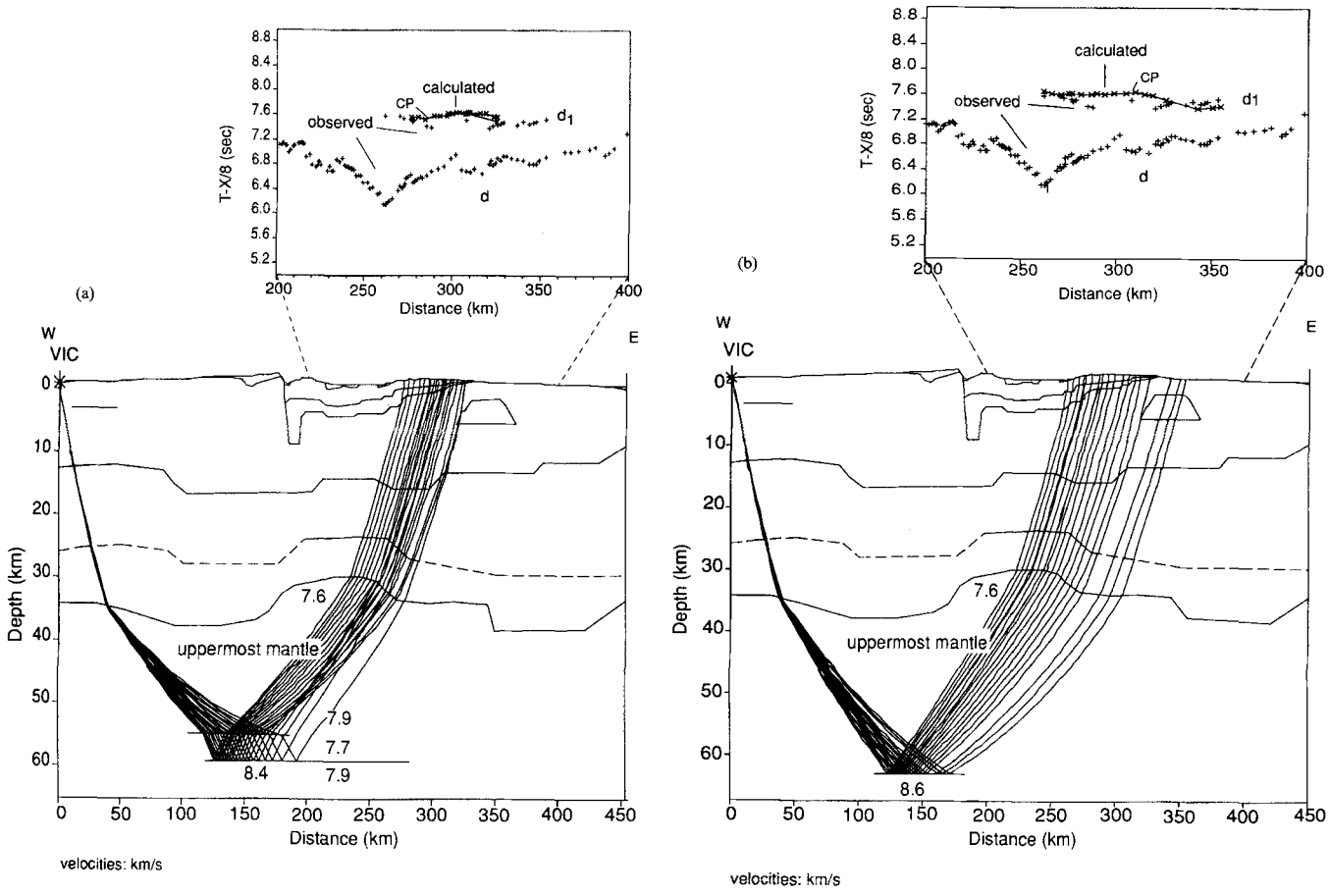

Figure 7. (a) Ray-trace diagram for the intramantle reflection d_1 for a model with a LVZ (bottom) and corresponding travel-time diagram (top). (b) Ray-trace diagram for the intramantle reflection d_1 for a model without a LVZ (bottom) and corresponding travel-time diagram (top).

flow values of about 50 mW m^{-2} are found on the rift flanks in Kenya with high but very variable values up to around 100 mW m^{-2} being limited to the rift-valley region (Morgan 1982; Nyblade *et al. 1990*; Wheildon *et al. 1994*). An average value of 40 mW m^{-2} was found on the western shoulder of the rift valley, north of the Nyanza Rift (Wheildon *et al.* 1994).

The pressure can be estimated (Mechie *et al.* 1994) for a velocity–depth function derived from the seismic model beneath the western rift flank as 17.1 kbar at 59 km depth or 18.4 kbar at 63 km depth. Errors caused by uncertainty in the pressure are thought unlikely to be significant, as a change of 2 kbar (equivalent to about 6 km change in depth) produces only a small change of about 0.02 km s^{-1} in *P*-wave velocity. In contrast, a 100 °C change in temperature produces a change of about 0.05 km s^{-1} in *P*-wave velocity.

The average mantle composition, P1 (Fig. 10) has been derived from xenoliths brought up by Quaternary volcanoes (Henjes-Kunst & Altherr 1992) and corresponds to a peridotite with 50 per cent olivine, 30 per cent orthopyroxene, 18 per cent clinopyroxene and 2 per cent spinel. At 63 km depth some garnet may be present at the expense of spinel, and taking into account that the spinel–garnet transition is likely to occur over a wide interval, a garnet peridotite, P3 (Fig. 11) consisting of 55 per cent olivine, 23 per cent orthopyroxene, 14 per cent clinopyroxene and 8 per cent garnet has also been modelled.

Combining a surface heat flow of 40–50 mW m^{-2} with the Pollack & Chapman (1977) geotherms leads to temperatures of around 600 °C at about 60 km depth. Even for such a low temperature, isotropic pure olivine has velocities of only 8.05 and 8.15 km s^{-1} for P1 and P3, respectively (Figs 10a and 11a). However, the velocity of either 8.4 km s^{-1} at 59 km depth or 8.6 km s^{-1} at 63 km depth beneath the western rift flank can be explained if preferred mineral orientation (anisotropy) is invoked. Involving anisotropy, either the transverse isotropic olivine model or the orthorhombic olivine model, is possible. In the case of the transverse isotropic model the faster '*a*' and '*c*' axes of the olivine should be randomly orientated in the horizontal plane. Although at temperatures as low as 600 °C at around 60 km depth both P1 and P3 have velocities of 8.3–8.4 km s^{-1}, compositions richer in olivine can have velocities up to 8.6 km s^{-1}, even at temperatures up to 800 °C (Figs 10b–c and 11b–c). In this respect it is interesting to note that kimberlites of uncertain age near the western end of the cross-rift line have brought up ultramafic xenoliths including olivine-rich harzburgites and dunites (Ito 1986). In the case of the orthorhombic model, the fast '*a*' axis of the olivine should be orientated along the direction of the cross-rift line. In the case of the model without a LVZ for both P1 and P3 at temperatures between 600° and 800 °C at 63 km depth, more than 75 per cent of the olivine must be preferentially orientated in order to attain a velocity of 8.6 km s^{-1}. For the model with a LVZ more than 50 per cent of the olivine must be preferentially orientated in order to attain a velocity of 8.4 km s^{-1} for both P1 and P3 at temperatures between 600 and 800 °C at 59 km

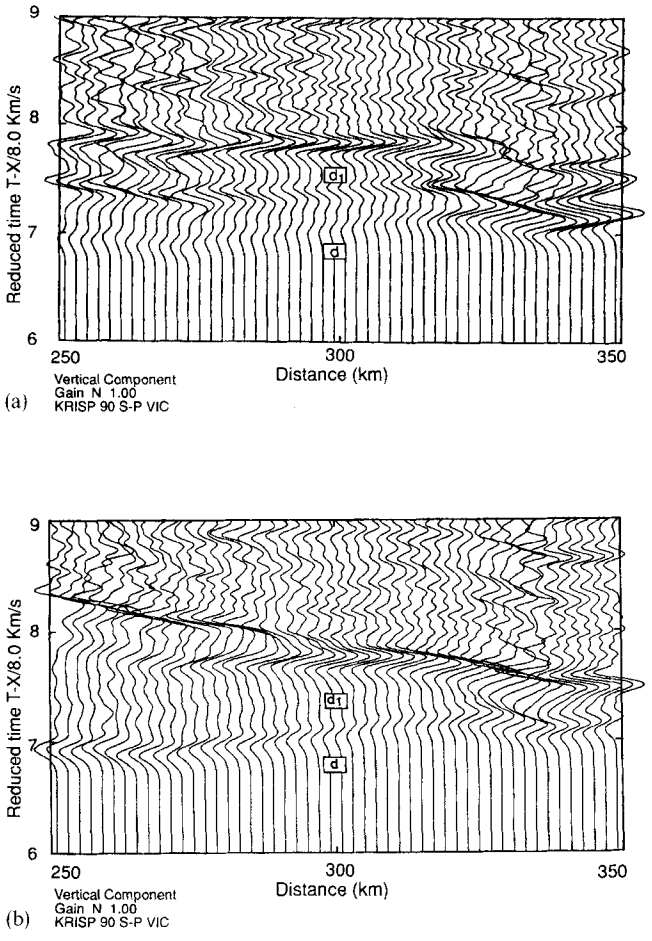

Figure 8. Synthetic seismograms for d and d_1 phases for the model with (top) and without (bottom) the LVZ, calculated by using a finite-difference technique (Sandmeier 1990).

depth. For compositions richer in olivine a smaller amount of the mineral is required to be preferentially orientated.

Keller *et al.* (1994) and Mechie *et al.* (1994) have also invoked anisotropy to explain high-velocity layers at 40–45 km and 60–65 km depth in the mantle below the axis of the northern part of the Kenya Rift. Their high velocities could be explained by either a transverse isotropic model similar to that utilized here or by an orthorhombic model in which the fast '*a*' axis of the olivine crystals is orientated along the rift axis. If the layer identified at 60–65 km depth beneath the rift axis and the layer identified here have a common origin, then either a transverse isotropic model or an orthorhombic model with the fast '*a*' axis of olivine orientated radially away from the apex of the Kenya dome could account for the observed seismic velocities. In either case, the cause of the anisotropy could be shear stress along more or less horizontal planes perpendicular to the slow '*b*' axis of olivine (Nicolas *et al.* 1971) and possibly directed radially away from the apex of the Kenya dome.

6 DISCUSSION

The upper-mantle seismic-velocity distribution beneath the western flank of the rift derived here is supported by both kinematic and dynamic modelling of the seismic wavefield and petrological modelling. Our proposed best-fitting model is

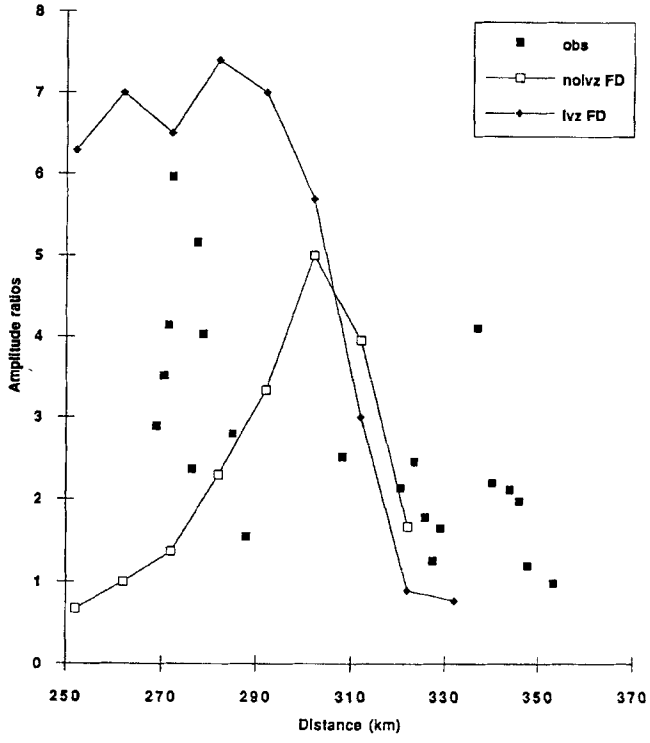

Figure 9. Comparison of observed and theoretical amplitude ratios for the model with and without the LVZ.

shown in Fig. 12(a). An alternative model can be envisaged with a LVZ between 55 and 59 km, and 8.4 km s^{-1} velocity underneath the LVZ (Fig. 7a). The implications are similar. For comparison, the axial-line model is also shown in Fig. 12(b). The reflector modelled at 63 km depth marks an increase in velocity to 8.6 km s^{-1}. This velocity is consistent with temperatures of 600–800 °C, a pressure of 18.4 kbar and a petrological model involving the presence of garnet and preferred orientation (anisotropy) of the olivine crystals either in a transverse isotropic or orthorhombic structure. Five points of note are detailed below.

6.1 An upper-mantle low-velocity zone

We cannot exclude the presence of a low-velocity zone in the uppermost mantle beneath the western flank of the rift. Low-velocity layers have been identified in the upper mantle beneath the axial line. The velocity inside the LVZ beneath the cross-rift line cannot be constrained because there is no reflection (with inverted polarity) seen from the top of the LVZ. The finite-difference synthetic-seismogram modelling provides similar amplitude ratios for the model with and without a LVZ. Petrological modelling requires relatively low temperatures that do not suggest the presence of melt at depth, but cannot exclude its presence laterally penetrating from the axial zone of the rift. Alternating high- and low-velocity layers have been found beneath the axis of the rift, where other geophysical results suggest the presence of anomalous mantle and partial melt. The low-velocity layers are present

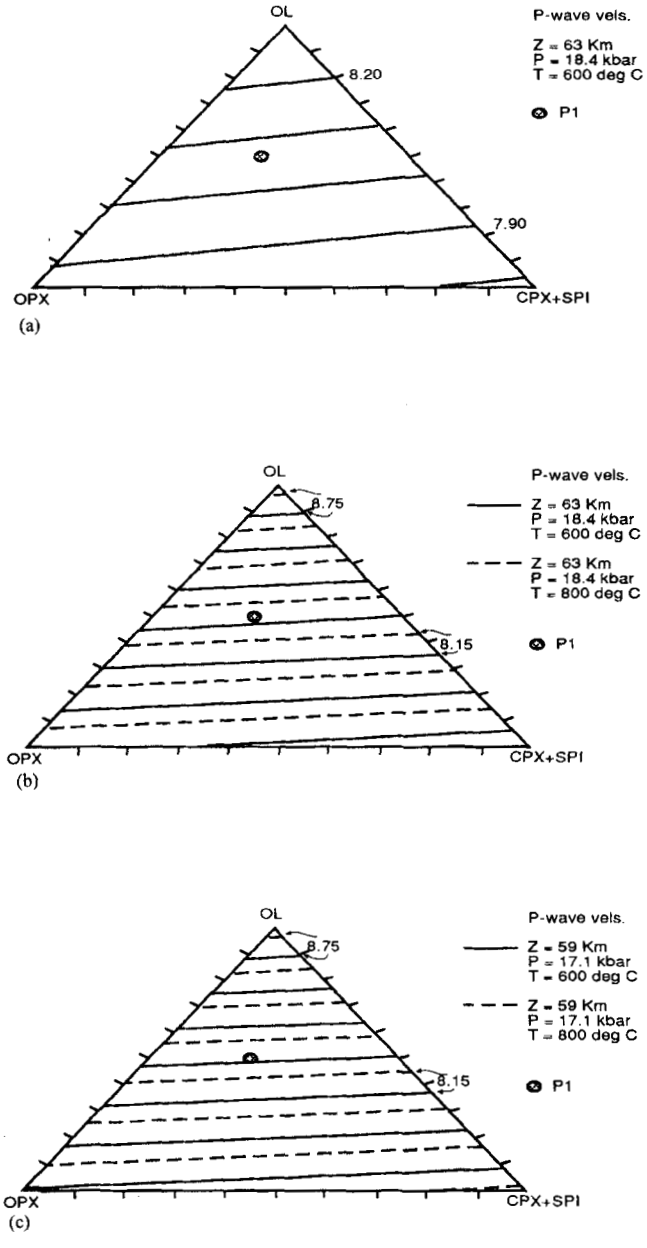

Figure 10. (a) Ternary diagram showing the relationship between *P*-wave velocity and mineralogical composition P1 for a pure isotropic model at 63 km depth. (b) Ternary diagram showing the relationship between *P*-wave velocity and mineralogical composition P1 for a transverse isotropic model at 63 km depth. (c) Ternary diagram showing the relationship between *P*-wave velocity and mineralogical composition P1 for a transverse isotropic model at 59 km depth. Note the similarity in the velocity for P1 between Fig. 10(b) and this figure.

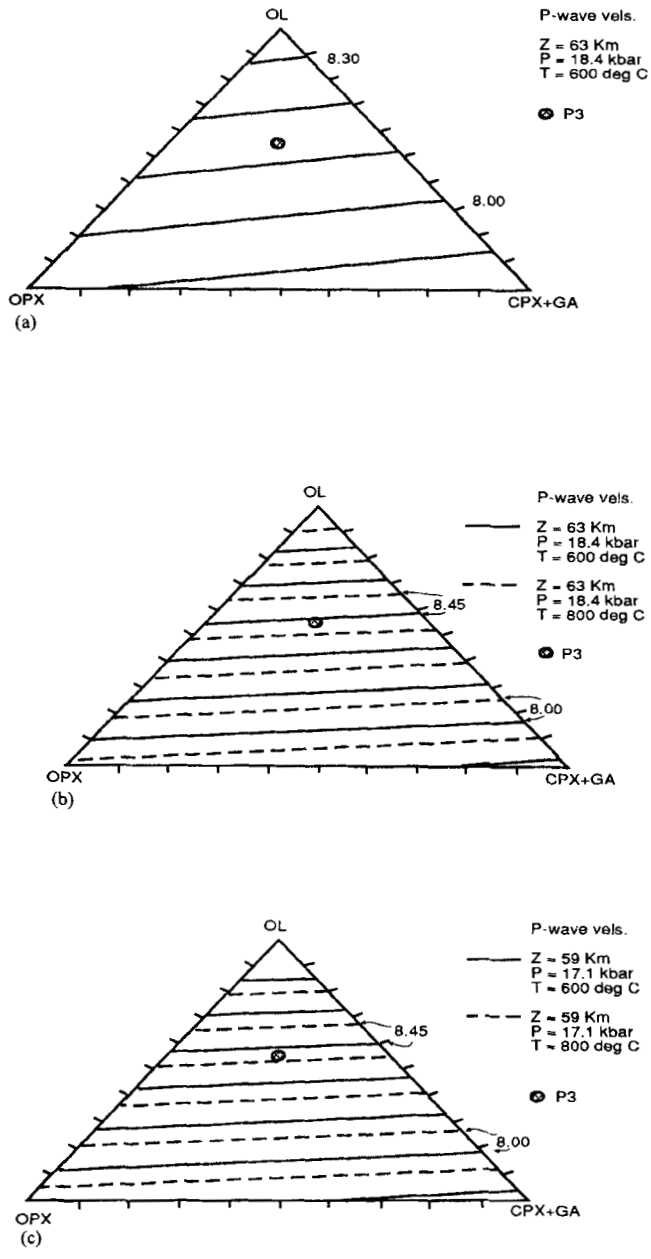

Figure 11. (a) Ternary diagram showing the relationship between *P*-wave velocity and mineralogical composition P3 for a pure isotropic model at 63 km depth. (b) Ternary diagram showing the relationship between *P*-wave velocity and mineralogical composition P3 for a transverse isotropic model at 63 km depth. (c) Ternary diagram showing the relationship between *P*-wave velocity and mineralogical composition P3 for a transverse isotropic model at 59 km depth. Note the similarity in the velocity for P3 between Fig. 11(b) and this figure.

below the northern part of the rift and do not extend as far south as the cross-rift line. Elsewhere beneath rifts or tectonically active areas, alternating high- and low-velocity layers have also been found (Prodehl 1981; Nagumo *et al.* 1981; Prodehl *et al.* 1992).

The following considerations are valid, assuming that the reflector seen under the western flank of the rift does not extend under the rift axis, and therefore the high velocity is limited to occur under the western flank of the rift:

(1) if the model with the LVZ is accepted, the anomalous mantle material occurring beneath the rift may extend laterally into this LVZ under the rift shoulder;

(2) if the model without the LVZ is accepted, the anomalous mantle material can be laterally constrained to exist beneath the surface expression of the rift.

We are inclined to prefer the second possibility because there is direct evidence for the presence of high velocities below

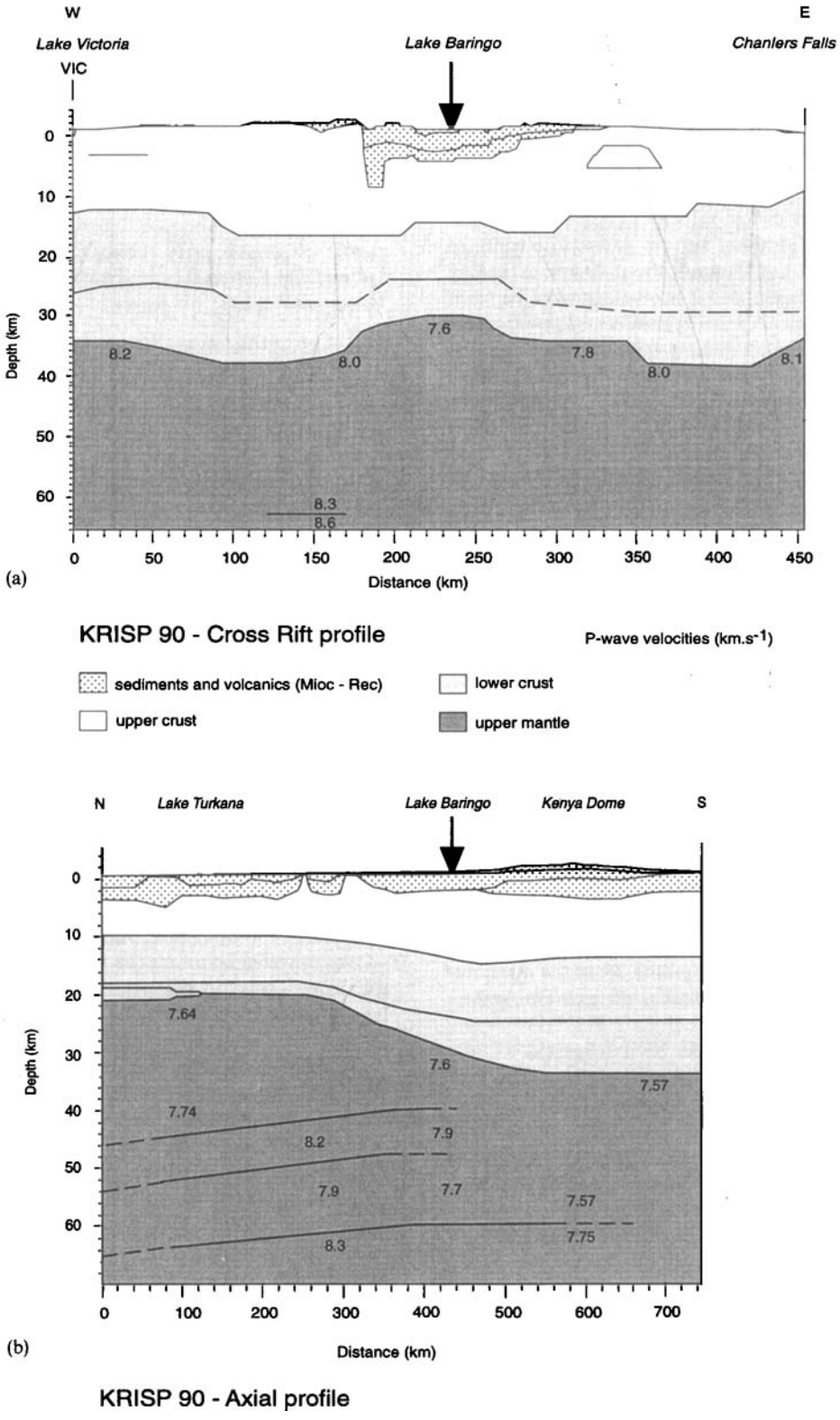

Figure 12. Velocity model of the cross-rift (top) and axial (bottom, distance-scale halved) profiles derived from ray-trace and synthetic-seismogram modelling. *P*-wave velocities are indicated in km s^{-1}.

the reflector, whereas there is no positive evidence for the LVZ above it. Also, there is scant evidence for the LVZ beneath Lake Baringo from the axial-line data.

6.2 Teleseismic results

The results from the KRISP 90 teleseismic survey (Achauer *et al.* 1994) show, in an east–west section through Lake Baringo, a narrow wedge of low-velocity material underneath the rift axis, broadening at about 100 km depth. The width of this zone at the depth of the Moho is about 20 km, extending to 30–40 km at 68 km depth, and it has velocities of between 7.5 and 7.8 km s^{-1} in the uppermost mantle. Such a pattern would fit the width of the anomalous mantle found here. It does not show (1) a thin layer of LVZ beneath the margin of the rift, and (2) high velocity values under the rift flank. However, (1) the depth resolution of the teleseismic results is not capable of resolving the thickness of the LVZ layer modelled here and (2) the proposed anisotropy results in the high velocity values being in the horizontal plane. These high velocities would not be seen by the rays inverted in the teleseismic analysis, which are supposed to have travelled along near-vertical paths in the direction of the slower '*b*' or '*c*' axes of olivine.

6.3 High velocity value/anisotropy

Examples of high velocities in upper-mantle material have been identified in regions surrounding other rifting areas. In the Jordan–Dead Sea Rift (Ginzburg *et al.* 1979) a discontinuity at a depth of 55 km within the upper mantle marks an increase in velocity to 8.6 km s^{-1}, a result obtained from seismic data recorded along the rift axis. In the Afar region, anisotropy in the mantle under the highlands surrounding the depression has been suggested to explain velocities higher than those beneath the depression itself (Gehlen, Forkel & Spies 1975). In the Baikal region, high velocities in the mantle have been explained by anisotropy in garnet pyrolite, from the interpretation of a seismic line across the Baikal rift axis (Burmakov *et al.* 1987).

Anisotropy in the mantle has also been suggested to exist in other geodynamic regions, where alternating high- and low-velocity layers have been found. In Fennoscandia (Cassell & Fuchs 1979) it has been suggested that shear stresses may create a preferred orientation of olivine crystals, which in turn would cause orientation of the maximum velocity direction.

6.4 Rifting or orogenic signature?

There is another intriguing possibility. The seismic line crosses the contact between the Archaean Nyanza Craton (ANC) and the Proterozoic Mozambique Orogenic Belt (MOB) approximately 70 km to the west of the rift's western bounding fault, in the vicinity of the Nandi fault. It is considered that the contact results from a Tibetan-style collisional orogen (Shackleton & Ries 1984; Berhe 1990).

It is possible that the upper-mantle discontinuity identified here is a pre-rift structure, resulting from that orogen; for example an intraplate shear zone, such as a décollement surface, or a relict oceanic or continental crustal eclogitic layer.

One of the clearest images of a subhorizontal reflector within the mantle at depths equivalent to those discussed here is seen beneath the DRUM deep reflection line across the Caledonides offshore NW Scotland. This line identified the 'W' reflector at a depth of 45–50 km (McGeary & Warner 1985). The reflector was interpreted initially as a detachment fault or décollement surface within the mantle resulting from the Caledonian orogeny, possibly reactivated during Mesozoic extension (Warner & McGeary 1987); subsequently it was interpreted as genetically linked to the Flannan reflection, produced from the top of a dipping 'relict oceanic and eclogitic component of a pre-Caledonian subduction zone within the lithospheric mantle' (Morgan *et al.* 1994). The correspondence between this and the Kenya Rift geological environment is striking.

6.5 Age of the anomalous mantle zone

The temperature distribution modelled from the velocity values could be used to give an indication of the age of anomalously hot mantle material beneath the rift axis. Turcotte & Schubert (1982) modelled the temperature effect of an intrusion on the surrounding material at different times after the initial intrusion to provide a way of constraining its age. However, even assuming a large initial temperature difference of 500 °C between the thermal anomaly and the surrounding lithosphere at about 35–45 km depth, even 20 Ma after the first appearance of the thermal anomaly the rise in temperature 20–30 km away from the anomaly would be only 200–300 °C. Such a temperature rise would cause a *P*-wave velocity decrease of only about 0.1–0.15 km s^{-1}. A better-constrained model, using also results for example from possible future deep-seismic-reflection profiling could allow this type of modelling to be applied to the upper mantle beneath the Kenya Rift.

7 CONCLUSION

In conclusion, an interface within the upper mantle beneath the western flank of the rift has been identified. Detailed analyses of the kinematic and dynamic characteristics of the seismic wavefield confirm the presence of a velocity of at least 8.4 km s^{-1} beneath the western flank of the rift. The petrological modelling suggests the following:

(1) relatively cool temperatures adjacent to the rift, beneath which partial-melt material has been predicted;

(2) the possibility of anisotropy in which the olivine crystal orientation is suggested as an explanation for the observed velocity structure. A further possibility is that the reflector is a pre-rift structure, resulting from the ANC–MOB contact.

All the evidence taken together suggests that the upper-mantle region of anomalously low-velocity material is confined to being below the surface expression of the rift itself, to a depth below 60 km. There is the possibility of a thin lateral intrusion immediately above the high-velocity layer, which has been shown to exist beneath the western flank at about this depth.

ACKNOWLEDGMENTS

We would like to acknowledge the assistance of the Kenya Government during the course of this project. KRISP was funded by the DFG (Germany), the NSF (USA), the EC and the NERC (UK). We thank Dr J. Luetgert of the USGS, Menlo Park, California for setting up the USGS wide-angle

software on the Geology Department Microvax at Leicester University and C. Abbott of Leicester University for writing the CANC filtering routine. We also thank Dr I. Hill of Leicester University for his useful suggestions during the processing and interpretation of the data and Dr A. Saunders of Leicester University for his constructive comments on the petrological modelling during the production of the manuscript. The synthetic seismogram calculations have been performed on the Siemens S600 supercomputer of the Computer Centre at Karlsruhe University. One of us (RM) was funded initially by a European Commission grant (Ref. no. 900009) and later by a British Council fellowship (Ref. ITA/2281/225/A).

REFERENCES

Achauer, U. and the KRISP Teleseismic Working Group 1994. New ideas on the Kenya Rift based on the inversion of the combined data set of the 1985 and 1989/90 seismic tomography experiments, in *Crustal and upper mantle structure of the Kenya Rift,* pp. 305–329, eds Prodehl, C., Keller, G.R. & Khan, M.A., *Tectonophysics,* **236**.

Ansorge, J., Blundell, D. & Mueller, S., 1992. Europe's lithosphere—seismic structure, in *A continent revealed: The European Geotraverse,* pp. 31–69, eds Blundell, D., Freeman, R. & Mueller, S., Cambridge University Press, Cambridge.

Berhe, S.M., 1990. Ophiolites in Northeast and East Africa: implications for Proterozoic crustal growth, *J. geol. Soc. Lond.,* **147,** 41–57.

Bhattacharji, F. & Koide, H., 1987. Theoretical and experimental studies of mantle upwelling, penetrative magmatism, and development of rifts in continental and oceanic crusts, *Tectonophysics,* **143,** 13–30.

Blundell, D., 1992. Integrated lithospheric cross section, in *A continent revealed: The European Geotraverse,* pp. 102–109, eds Blundell, D., Freeman, R. & Mueller, S., Cambridge University Press, Cambridge.

Burmakov, Ju.A., Chernyshev, N.M., Vinnik, L.P. & Yegorkin, A.V., 1987. Comparative characteristic of the lithosphere of the Russian platform, the West Siberian platform and the Siberian platform from seismic observations on long-range profiles, *Am. geophys. Un. Geodyn. Series,* **17,** 175–189.

Cassell, B.R. & Fuchs, K., 1979. Seismic investigations of the subcrustal lithosphere beneath Fennoscandia, *J. Geophys.,* **46,** 369–384.

Červený, V., 1985. Ray synthetic seismograms for complex two-dimensional and three-dimensional structures, *J. Geophys.,* **58,** 2–26.

Červený, V. & Pšenčík, I., 1981. *A guide to the program SEIS81,* Charles University, Prague.

Červený, V. & Pšenčík, I., 1984. A brief description of program package SEIS81, used to compute data set 1, model Zurich, in *Interpretation of seismic wave propagation in laterally heterogeneous structures,* pp. 40–47, eds Finlayson, D.M. & Ansorge, J., Workshop Proceedings, Rep. 258, Bureau of Mineral Resources, Geology and Geophysics, Canberra.

Červený, V., Molotkov, I.A. & Pšenčík, I., 1977. *Ray method in seismology,* Charles University, Prague.

Fuchs, K., 1983. Recently formed elastic anisotropy and petrological models for the continental subcrustal lithosphere in southern Germany, *Phys. Earth planet. Inter.,* **31** , 93–118.

Gehlen, K.V., Forkel, W. & Spies, O., 1975. Petrological interpretation of geophysical data from the Afar Depression, Ethiopia, in *Afar Depression in Ethiopia,* pp. 151–155, eds Pilger, A. & Rosler, A., Schweizerbart, Stuttgart.

Ginzburg, A., Makris, J., Fuchs, K., Perathoner, B. & Prodehl, C., 1979. Detailed structure of the crust and upper mantle along the Jordan–Dead Sea Rift, *J. geophys. Res.,* **84** , 5605–5612.

Green, W.V., Achauer, U. & Meyer, R.P., 1991. A three-dimensional seismic image of the crust and upper mantle beneath the Kenya Rift, *Nature,* **354,** 353–357.

Hattingh, M., 1988. A new data adaptive filtering program to remove noise from geophysical time- or space-series data, *Computers Geosci.,* **14,** 467–480.

Henjes-Kunst, F. & Altherr, R., 1992. Metamorphic petrology of xenoliths from Kenya and Northern Tanzania and implications for geotherms and lithospheric structure, *J. Petrol.,* **33** , 1125–1156.

Henry, W.J., 1987. A seismic investigation of the Kenya Rift Valley, *PhD thesis,* University of Leicester.

Hirn, A., Steinmetz, L., Kind, R. & Fuchs, K., 1971. Long range profiles in Western Europe: II. Fine structure of the lower lithosphere in France (Southern Bretagne), *Z. Geophysik,* **39** , 363–384.

Ito, M., 1986. Kimberlites and their ultramafic xenoliths from western Kenya, *TMPM Tschermaks Min. Petr. Mitt.,* **35,** 193–216.

Keller, G.R., Mechie, J., Braile, L., Mooney, W.D. & Prodehl, C., 1994. Seismic structure of the uppermost mantle beneath the Kenya Rift, in *Crustal and upper mantle structure of the Kenya Rift,* pp. 201–216, eds Prodehl, C., Keller, G.R. & Khan, M.A., *Tectonophysics,* **236**.

Kelly, K.R., Ward, R.W., Treitel, S. & Alford, R.M., 1976. Synthetic seismograms: A finite-difference approach, *Geophysics,* **41,** 2–27.

Kind, R., 1974. Long-range propagation of seismic energy in the lower lithosphere, *J. Geophys.,* **40,** 189–202.

Kirk, W.J., 1989. Seismic and potential field studies over the East Midlands, *PhD thesis,* University of Leicester.

Luetgert, J.H., 1992. MacRay—Interactive two-dimensional seismic raytracing for the Macintosh, US geol. Surv. Open-File Rep. 92–356.

Maguire, P.K.H., Swain, C.J., Masotti, R. & Khan, M.A., 1994. A crustal and uppermost mantle cross-sectional model of the Kenya Rift derived from seismic and gravity data, in *Crustal and upper mantle structure of the Kenya Rift,* pp. 217–249, eds Prodehl, C., Keller, G.R. & Khan, M.A., *Tectonophysics,* **236**.

Makris, J. & Ginzburg, A., 1987. The Afar Depression: transition between continental rifting and sea-floor spreading, *Tectonophysics,* **141,** 199–214.

McGeary, S. & Warner, M.R., 1985. Seismic profiling the continental lithosphere, *Nature,* **317,** 795–797.

Mechie, J., Prodehl, C. & Koptschalitsch, G., 1986. Ray-path interpretation of the crustal structure beneath Saudi Arabia, *Tectonophysics,* **131,** 333–352.

Mechie, J., Fuchs, K. & Altherr, R., 1994. The relationship between seismic velocity, mineral composition and temperature and pressure in the upper mantle—with an application to the Kenya Rift and its eastern flank, in *Crustal and upper mantle structure of the Kenya Rift,* pp. 453–464, eds Prodehl, C., Keller, G.R. & Khan, M.A., *Tectonophysics,* **236**.

Mereu, R.F., 1967. Curvature corrections to upper mantle seismic refraction surveys, *Earth planet. Sci. Lett.,* **3,** 7–42.

Mooney, W.D., Gettings, W.E., Blank, R.H. & Healy, J.H., 1985. Saudi Arabian seismic-refraction profile: A traveltime interpretation of crustal and upper mantle structure, *Tectonophysics,* **11,** 173–246.

Morgan, P., 1982. Heat flow in rift zones, in *Continental and Oceanic Rifts,* pp. 107–122, ed. Palmason, G., Am. geophys. Un. Geodyn. Series, **8,** Washington, DC.

Morgan, J.V., Hadwin, M., Warner, M.R., Barton, P.J. & Morgan, R.P.L., 1994. The polarity of deep seismic reflections from the lithospheric mantle: evidence for a relict subduction zone, *Tectonophysics,* **232,** 319–328.

Nagumo, S., Ouchi, T., Kasahara, J. & Koresawa, S., 1981. Sub-Moho seismic profile in the Mariana Basin—Ocean bottom seismograph long-range explosion experiment, *Earth planet. Sci. Lett.,* **53,** 93–102.

Nicolas, A., Bouchez, F., Boudier, F. & Mercier, J.C., 1971. Textures, structures and fabrics due to solid state flow in some European lherzolites, *Tectonophysics,* **12,** 55–86.

Nyblade, A.A., Pollack, H.N, Jones, D.L., Podmore, F. & Mushayandebvu, M., 1990. Terrestrial Heat Flow in East and Southern Africa, *J. geophys. Res.,* **95,** 17 371–17 384.

Pollack, H.N. & Chapman, D.S., 1977. On the regional variation of

heat flow, geotherms, and lithospheric thickness, *Tectonophysics,* **38,** 279–296.

Prodehl, C., 1981. Structure of the crust and upper mantle beneath the central European rift system. in *The Dead Sea Rift,* pp. 255–269, eds Freund, R. & Garfunkel, Z., *Tectonophysics,* **80.**

Prodehl, C., 1985. Interpretation of a seismic-refraction survey across the Arabian Shield in western Saudi Arabia, *Tectonophysics,* **111,** 247–282.

Prodehl, C., Mueller, S., Glahn, A., Gutscher, M. & Haak, V., 1992. Lithospheric cross sections of the European Cenozoic rift system, in *Geodynamics of Rifting. Case History Studies on Rifts: Europe and Asia,* Vol. 1., pp. 113–138, ed. Ziegler, P.A., *Tectonophysics,* **208.**

Prodehl, C., Jacob, A.W.B., Thybo, H., Dindi, E. & Stangl, R., 1994. Crustal structure on the northeastern flank of the Kenya Rift, *in Crustal and upper mantle structure of the Kenya Rift,* pp. 271–290, eds Prodehl, C., Keller, G.R. & Khan, M.A., *Tectonophysics,* **236.**

Sandmeier, K.-J., 1990. Untersuchung der Ausbreitungseigenschaften seismischer Wellen in geschichteten und streuenden Medien, *PhD thesis,* Universität Karlsruhe.

Shackleton, R.M. & Ries, A.C., 1984. The relation between regional consistent strecthing lineations and plate motions, *J. struct. Geol.,* **6,** 111–117.

Turcotte, D.L. & Schubert, G., 1982. *Geodynamics—Applications of Continuum Physics to Geological Problems,* J. Wiley & Sons, New York.

Warner, M. & McGeary, S., 1987. Seismic reflection coefficents from mantle fault zones, *Geophys. J. R. astr. Soc.,* **89,** 223–230.

Wheildon, J., Morgan, P., Williamson, K.H., Evans, T.R. & Swanberg, C.A., 1994. Heat flow in the Kenya rift zone, *in Crustal and upper mantle structure of the Kenya Rift,* pp. 131–149, eds Prodehl, C., Keller, G.R. & Khan, M.A., *Tectonophysics,* **236.**

Widrow, B. & Hoff, M., 1960. Adaptive switching circuits , *IRE Wescon Conv. Rec.,* **4,** 96–104.

Widrow, B. *et al.* 1975. Adaptive noise cancelling: Principles and applications, *Proc. IEEE,* **63,** 1692–1716.

Widrow, B., McCool, J.M., Larimore, M.G. & Johnson, C.R., 1976. Stationary and nonstationary characteristics of the LMS adaptive filter: *Proc. IEEE,* **64,** 1151–1162.